arXiv:1607.03001v1 [quant-ph] 11 Jul 2016

Temporal-mode tomography of single photons

Vahid Ansari,[1,*] Markus Allgaier,[1] Linda Sansoni,[1] Benjamin Brecht,[1,2]
Jonathan Roslund,[3] Nicolas Treps,[3] Georg Harder,[1] and Christine Silberhorn[1]

[1] *Integrated Quantum Optics, Paderborn University, Warburger Strasse 100, 33098 Paderborn, Germany*
[2] *Clarendon Laboratory, Department of Physics, University of Oxford, Parks Road, OX1 3PU, United Kingdom*
[3] *Laboratoire Kastler Brossel, UPMC-Sorbonne Universités, CNRS, ENS-PSL Research University, Collége de France; CC74, 4 Place Jussieu, 75252 Paris, France*

(Dated: July 12, 2016)

We employ a tailored sum-frequency generation process, the quantum pulse gate (QPG), to perform arbitrary projective measurements on the temporal modes (TMs) of genuine non-classical states. To prepare non-classical states, we herald both spectrally pure and mixed single photons from a tailored parametric down-conversion source (PDC). Using mutually unbiased bases, we reconstruct the density matrix of the single photons up to 11 dimensions, thus revealing all information about their TM structure. This work constitutes a step towards exploiting TMs of single photons for quantum information science.

Introduction - Field-orthogonal temporal modes (TMs) span the frequency-space of optical states, which alongside polarization, spatial and photon-number degrees of freedom fully describes light. Naturally, TMs provide an intrinsically unbounded Hilbert space for diverse applications in quantum information science. Compatibility of TMs with single-mode fibers provides a promising framework for implementation of high-dimensional quantum communication protocols [1]. Harnessing TMs in quantum information science has been the subject of different studies. It has been proposed that TMs can facilitate the realization of a deterministic controlled-sign gate [2], provide an interface between optical quantum states and stationary quantum memories [3, 4] and enhance the resolution of stimulated Raman spectroscopy [5].

The challenge is to manipulate and measure TMs in a way that preserves the quantum properties of the state. More precisely, operations on TMs need to work with high efficiencies on a single-photon and preserve their orthogonality. A promising candidate to achieve these goals is the quantum pulse gate (QPG) [6–10], an engineered sum-frequency process. It is designed to operate on arbitrary TMs, set by the classical pump of the process. A QPG can be used to encode information into TMs by shaping single photons as well as performing measurements on well defined TMs. Here, as a first step towards such applications, we demonstrate a full TM tomography of quantum states with a QPG.

In general, spectral characterization at the single-photon level requires interferometric techniques with a known reference field. Two well-known examples are spectral interferometry for classical light [11, 12] and homodyne detection for quantum light. Recent work based on homodyne detection has demonstrated the use of TMs for continuous variable experiments [13]. However, homodyne detection is limited to Gaussian operations. The advantage of a QPG is that it can be combined with any detection scheme, including non-Gaussian measurements and direct detection of single photon states and entangled photon-pair states.

In this Letter, we use a QPG together with a single-photon detector to perform projective TM measurements on single photons. We use mutually unbiased bases (MUBs) in 5 and 11 dimensions to experimentally reconstruct the full density matrix of single photons in a pure or partially mixed state, heralded from a tailored parametric down-conversion source (PDC). We start by describing our source of single photons, then we present a formalism to use the QPG as a tool for TM tomography and finally we show the experimental results of quantum state tomography.

Single photon source - To generate quantum states, we use a type II PDC process, described by the Hamiltonian

$$\hat{H}_{\mathrm{PDC}} \propto \iint f(\omega_{\mathrm{s}},\omega_{\mathrm{i}})\hat{b}^{\dagger}(\omega_{\mathrm{s}})\hat{c}^{\dagger}(\omega_{\mathrm{i}})d\omega_{\mathrm{s}}d\omega_{\mathrm{i}} + \mathrm{h.c.}, \quad (1)$$

where $\hat{b}^{\dagger}(\omega_{\mathrm{s}})$ and $\hat{c}^{\dagger}(\omega_{\mathrm{i}})$ are the standard creation operators for signal and idler fields at frequencies ω_{s} and ω_{i}. The joint spectral amplitude (JSA) function $f(\omega_{\mathrm{s}},\omega_{\mathrm{i}})$ describes the spectral phase and amplitude of the created state and can be greatly tailored by exploiting the dispersion properties of the crystal and shape of the pump pulse [14–17]. Performing a Schmidt decomposition of the JSA function, we can expand it into orthonormal modes ψ_k and ϕ_k [18], with eigenvalues $\sqrt{\gamma_k}$,

$$f(\omega_{\mathrm{s}},\omega_{\mathrm{i}}) = \sum_k \sqrt{\gamma_k}\psi_k(\omega_{\mathrm{s}})\phi_k(\omega_{\mathrm{i}}). \quad (2)$$

This expansion gives a natural, discrete basis for the PDC process. For a Gaussian JSA, this decomposition yields Hermite-Gaussian functions as eigenmodes, which motivates our later choice of Hermite-Gaussian functions as the TM basis for state tomography.

In the single-photon limit, i.e. for low pump powers of

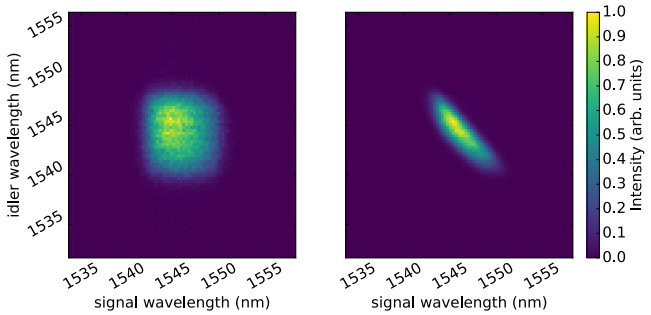

FIG. 1. Measured JSI of PDC states. Left: Single-mode state with Schmidt number K=1.01. Right: Multimode state with K=1.96. The spectrum of each PDC photon is merely filtered by bandpass filters to suppress background noises.

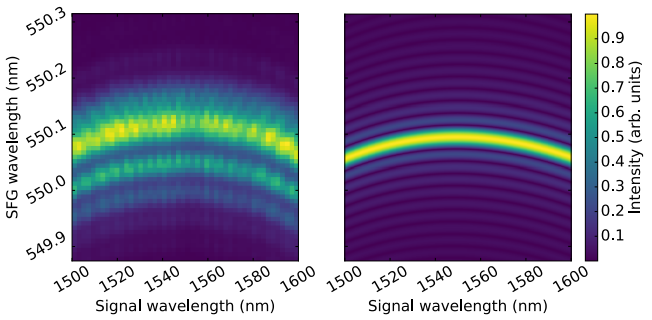

FIG. 2. Phasematching function of the QPG waveguide. Left: Experimentally measured. Right: Numerically modeled. The zero gradient of the phasematching curve is an indicator of group-velocity matching between input signal and the pump field. Imperfections in the measured phasematching curve are due to inhomogeneities of the waveguide and poling period.

the PDC source, the resulting state becomes

$$|\Psi\rangle \propto |0\rangle + \lambda \sum_k \sqrt{\gamma_k} \hat{B}_k^\dagger \hat{C}_k^\dagger |0\rangle + ..., \tag{3}$$

where we introduced the TMs $\hat{B}_k^\dagger = \int \psi_k(\omega_\mathrm{s}) \hat{a}_\mathrm{s}^\dagger(\omega_\mathrm{s}) \mathrm{d}\omega_\mathrm{s}$ and $\hat{C}_k^\dagger = \int \phi_k(\omega_\mathrm{i}) \hat{a}_\mathrm{i}^\dagger(\omega_\mathrm{i}) \mathrm{d}\omega_\mathrm{i}$. The parameter λ is the gain of the nonlinear process and assumed to be small here such that higher photon number components can be neglected. If we condition our measurement upon a detection of an idler photon, we herald a single photon in the signal mode. This is the photon we perform tomography on.

The Schmidt decomposition uniquely describes the structure of spectral correlations in bipartite systems. The number of Schmidt modes in the system can be quantified as $K \equiv 1/\sum_k \gamma_k^2$, known as the Schmidt number [19, 20], and quantifies the strength of spectral correlations. A Schmidt number of 1 corresponds to a single-mode state. In practice, it is possible to control the number of created Schmidt modes by spectral shaping of the pump field of the PDC process [1, 16]. Eq. (3) clearly shows that if we detect a signal photon in mode $\hat{B}_k$, the idler photon will certainly be in the corresponding mode $\hat{C}_k$. However, our heralding scheme is insensitive to the TM of the idler, such that the heralded state becomes a mixture

$$\hat{\rho} = \sum_k \gamma_k |B_k\rangle \langle B_k|, \tag{4}$$

where $|B_k\rangle = \hat{B}_k^\dagger |0\rangle$.

In this work, we use two different pump configurations that correspond to either single-mode or multimode PDC [16]. The multimode state populates several TMs, making it more exciting for tomography. The states are created inside a 6 mm long periodically poled KTP waveguide pumped with Gaussian pulses centered at 772 nm with intensity full-width-at-half-maximum of either 3 nm or 0.8 nm to create spectrally single-mode or multimode PDC states, respectively [16]. The corresponding measured joint spectral intensities (JSIs) $|f(\omega_s, \omega_i)|^2$ are plotted in Fig. 1. They are measured with a time-of-flight spectrometer [16, 21], consisting of dispersive fibers and time resolved single-photon detection with spectral resolution 0.25 nm.

Concerning the two-photon components, we pump the source with a low pump-pulse energy of 62 pJ. In this configuration, we measure a heralded second-order correlation function [22] of $g^{(2)} = 0.20 \pm 0.06$, indicating that two-photon contributions are relatively low, of the order of 10 %.

Quantum pulse gate- A frequency-conversion process is described by the Hamiltonian

$$H_\mathrm{FC} \propto \iint f_\mathrm{FC}(\omega_\mathrm{in}, \omega_\mathrm{out}) \hat{a}^\dagger(\omega_\mathrm{in}) \hat{d}(\omega_\mathrm{out}) d\omega_\mathrm{in} d\omega_\mathrm{out} + \mathrm{h.c.}. \tag{5}$$

Analogous to the PDC process, the spectral properties can be analyzed by performing a Schmidt decomposition of $f_\mathrm{FC}(\omega_\mathrm{in}, \omega_\mathrm{out})$. Under certain conditions, which we discuss later, the Hamiltonian reduces to a beamsplitter operating on single broadband modes:

$$H_\mathrm{QPG} = i\theta(\hat{A}_k^\dagger \hat{D} - \hat{A}_k \hat{D}^\dagger), \tag{6}$$

where mode $\hat{A}_k$ can be set by the mode of the pump and mode $\hat{D}$ is given by the phasematching of the crystal. The beamsplitter parameter θ scales with pump power as $\theta \propto \sqrt{P}$.

The key condition to achieve single-mode operation as given by the Hamiltonian in Eq. (6) of the QPG is group-velocity matching between the pump and the input signal [7]. To find the optimum group-velocity matching, we measure the phasematching function of the QPG waveguide for the SFG process in our wavelength range of interest, using a bright, tunable continuous-wave input laser. In Fig. 2, we plot the numerically modeled

and experimentally measured phasematching functions. The gradient of the phasematching curve is directly related to the group-velocity mismatch between the input signal and the pump field. At the top of the phasematching curve, where the gradient is zero, we have an ideal group-velocity matching condition. For our measurements we choose the bandwidth of the QPG pump and PDC photons to be in a window smaller than 10 nm centered at 1546 nm which provides an optimal group-velocity matching.

Tomography - Now we combine the single photon source and the QPG to perform quantum state tomography. Our goal is to fully characterize the spectral properties of a single photon, described by its density matrix

$$\hat{\rho} = \sum_{i,j} \rho_{ij} \left|i\right\rangle \left\langle j\right|, \tag{7}$$

where $\{|i\rangle\}$ describes an orthonormal TM basis. We choose a Hermite-Gaussian basis $|i\rangle = \int \mathrm{d}\omega \; h_i(\omega) \, |\omega\rangle$, where h_i are Hermite-Gaussian functions of order i, centered at the central frequency of the PDC photons. In principle, any choice of basis is valid at this point. However, we adapt the tomography basis to the TMs of the input single photons, such that the density matrix has a simple low-dimensional representation.

The QPG in combination with a single-photon detector effectively performs a projective measurement $\langle A_k| \, \hat{\rho} \, |A_k\rangle$. We can choose the TMs of the QPG, A_k, by shaping the spectrum of the pump, thus generating a complete set of positive operator valued measures (POVM) $\hat{\Pi}_k = |A_k\rangle \langle A_k|$. Quite unusual for a quantum-optical experiment, we are free to choose any POVMs we like. This is due to the structure of the Hamiltonian in Eq. (6). The ideal set for a tomographic measurement is a maximal set of MUBs [23, 24]. The construction of MUBs is known in any dimension d that is a power of a prime number, which is sufficient for our purposes. Then, it is possible to construct $d+1$ orthonormal bases, such that the overlap between two vectors from different bases is always $1/d$. This results in $d(d+1)$ states $|A_k\rangle$ and their corresponding POVMs.

Having established the concept of the measurement, let us move to the experimental realization. A schematic layout of the experimental setup is shown in Fig. 3. We use the PDC source as described earlier.

The PDC photons (signal and idler) with orthogonal polarization are separated on a polarizing beamsplitter, after which the idler photon is directly coupled into a single-mode fiber to be detected as a herald and the signal photon is directed to the QPG. The heralded single photon, together with a strong pump field at 854 nm, is then coupled to a home-built 27 mm long periodically poled lithium niobate (PPLN) waveguide where they interact in a group-velocity matched sum-frequency generation (SFG) process. We use a liquid-crystal-based

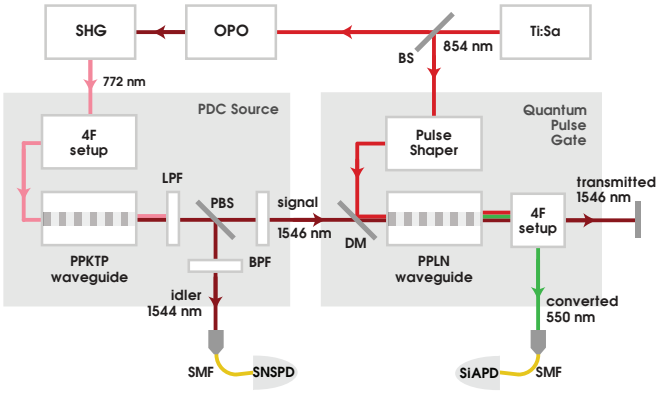

FIG. 3. A titanium:sapphire (Ti:Sa) oscillator (854 nm, 150 femtosecond, 80 MHz) is used to pump the optical parametric oscillator (OPO) and second-harmonic generator (SHG). Spectral bandwidth of the SHG field is shaped by a dispersion-free 4F-setup and is the coupled to a periodically poled potassium titanyl phosphate (PPKTP) waveguide. We use a long-pass filter (LPF) and 8 nm broad bandpass filters (BPF) to filter out the pump and other background noises from PDC photons. The PDC photons are split on a polarizing beamsplitter and either coupled to single-mode fiber (SMF) or redirected to the QPG setup. In the QPG setup a tap-off of the Ti:Sa laser from a beamsplitter (BS) is sent to the SLM pulse shaper setup. Then the pump at 854 nm and PDC photon at 1546 nm are combined on a dichroic mirror (DM) and coupled to a home-built periodically poled lithium niobate (PPLN) waveguide, held at 160°C. After the PPLN waveguide, the SFG and unconverted PDC photons are separated by a 4F-setup and are coupled to SMFs. Eventually SMFs conveying PDC photons are connected to superconducting nanowire single-photon detectors (SNSPD) and SMF for green photons is connected to a silicon avalanche photodiode (SiAPD).

spatial-light-modulator (SLM) setup, with a spectral resolution of 0.05 nm [25], to shape the spectral amplitude and phase of the pump field. At the output port of the waveguide, we separate the pump, the transmitted signal and the output SFG in a 4F-setup and we couple each beam into a single-mode fiber. As detectors, we use fiber-coupled, superconducting nanowire single-photon detectors (SNSPDs) for the PDC photons and a silicon avalanche photodiode (APD) for the upconverted green photons.

For the tomographic analysis of the heralded PDC photons, we employ a space of 5 and 11 dimensions, spanned by Hermite-Gaussian modes adapted to the central frequency and bandwidth of the PDC photons. In practice, performing tomography in dimension 5 is sufficient for our single photon states. However, we expand the dimensionality to 11 to show the scalability of our tomography method. To find the adapted frequency and bandwidth, we use the method presented in [9]. We record single-photon clicks at the converted output of the QPG, heralded by the PDC idler photons. After recording click rates c_ν corresponding to each projective measurement

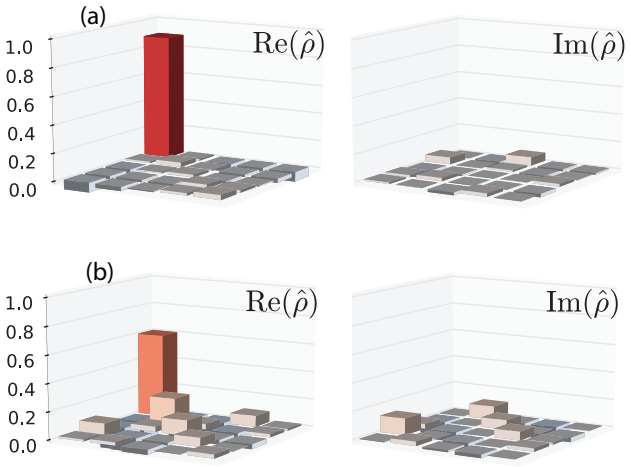

FIG. 4. Reconstructed density matrices in 5 dimensional space. (a) Real and imaginary parts of the density matrix for a pure single-mode state. (b) Real and imaginary part of the density matrix for a partially mixed multimode state.

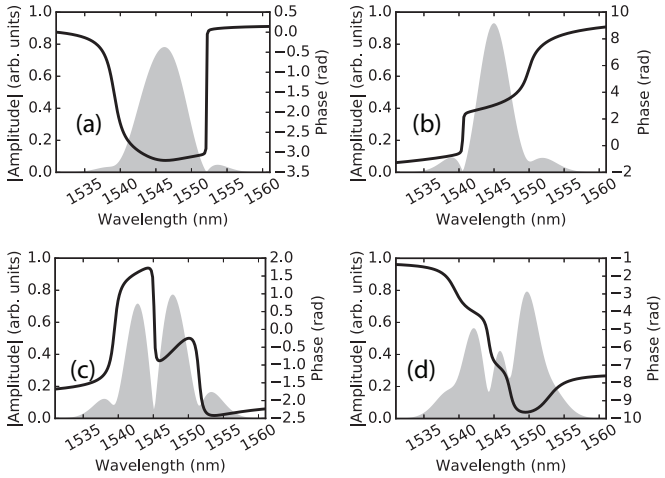

FIG. 5. Eigenmodes of measured density matrices. (a) The first eigenmode of the density matrix corresponding to single-mode state. (b), (c) and (d) are first three eigenmodes of the multimode density matrix. The shaded gray area is the spectral amplitude and solid black line is the spectral phase.

with a measurement time of five seconds, we normalize them over the pump power to acquire the projection probabilities n_ν. This normalization is necessary since the SLM pulse shaper has different output powers for different pulse shapes. For this reason, we stay in a low pump-power regime, where the conversion efficiency is $\eta_{\mathrm{QPG}} \propto \sin^2(\theta) \approx P$ [9]. This allows us to normalize count rates with respect to the pump power, without characterizing precisely the efficiency of the process. In principle, the QPG can also operate at high conversion efficiencies [9, 26].

To reconstruct the optimal density matrix, using the maximum-likelihood technique [27], we minimize the sum of square distances:

$$\min_{\rho} \sum_{\nu} \frac{(n_\nu - \langle\psi_\nu|\,\hat{\rho}\,|\psi_\nu\rangle)^2}{\sigma_\nu^2} \tag{8}$$

We take into account physical constraints on ρ and statistical uncertainties σ_ν, estimated from the count rates by assuming Poissonian click rates.

In Fig. 4(a) and Fig. 4(b) we show the density matrix of *single-mode* and *multimode* heralded PDC states. From the JSI in Fig. 1 we expect pure states in the first case and slightly mixed states in the second case [15]. Indeed, this is in agreement with the reconstructed density matrices, which feature mainly one component in the first case, and decaying diagonals in the second case.

To find a better understanding of the TM structure, we calculate the eigenmodes of the density matrices and plot them in the frequency basis, as shown in Fig. 5. Note that Fig. 5(a) shows the main mode of the pure-state density matrix, while Figs. 5(b,c,d) show the first three modes of the mixed-state density matrix. The corresponding eigenvalues of the latter are 0.773, 0.164, and 0.061. Comparing the main modes of the pure-state and mixed-state density matrices, we observe that the mode becomes narrower in the mixed case which is expected from the JSI of the PDC state. The bandwidth mismatch of the eigenmodes of the mixed-state and the tomographic basis can also be directly seen in the population of off-diagonal elements in the density matrix. The shape of the eigenmodes resembles Hermite-Gaussian modes, again as expected for the PDC process. For instance, in Fig. 5 (c), we can see the phase jump

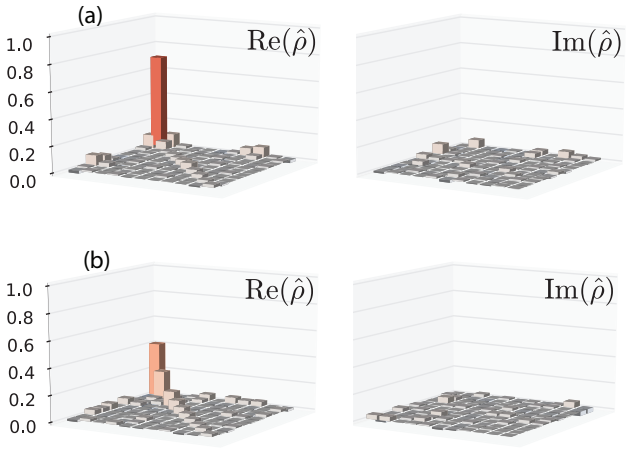

FIG. 6. Reconstructed density matrices in 11 dimensional space. (a) Real and imaginary parts of the density matrix for a pure single-mode state. (b) Real and imaginary part of the density matrix for a partially mixed multimode state.

of π at the center of the mode, associated with the first order Hermite-Gaussian function. However, the eigenmodes reveal slight deviations in the amplitudes as well as the phase profiles of the modes, which is expected for a real PDC source.

From the density matrices we calculate the purities $P = \mathrm{Tr}(\rho^2)$ to be 0.83 and 0.63 for the two cases, respectively. The reduction from unity purity in the first case can be attributed to the generated PDC state as well as experimental imperfections in the tomography. A further study of the QPG in the spirit of process tomography is required to understand the limits and imperfections of the method. One possible route in this direction is to implement a second QPG as a quantum pulse shaper, allowing to generate single photons in arbitrary TMs.

The reconstructed density matrices of the same input states but in an 11-dimensional space are shown in Fig. 6. In this case, we obtain purities of 0.60 and 0.31 for single-mode and multimode states, respectively. We attribute the lower purities in the higher-dimensional tomographic basis to experimental imperfections such as the limited resolution of the SLM-setup, that can compromise the orthogonality of the tomographic basis. While these imperfection are also present in the 5 dimensional case, their effect on the purity increases with higher dimensions. Regarding the density matrices themselves, the qualitative behavior is in very good agreement with the 5-dimensional case and shows that TM tomography in the manner presented in this paper can be directly extended to higher dimensions.

In conclusion, we have demonstrated TM tomography in 5 and 11 dimensions by reconstructing the density matrices of pure and mixed single photons. This lays the foundation for generation and measurement of arbitrary TMs, which is a first step towards high-dimensional quantum information science with TMs.

Acknowledgment - This research has received funding from the Deutsche Forschungsgemeinschaft (DFG) via Sonderforschungsbereich TRR 142, the Gottfried Wilhelm Leibniz-Preis and from the European Unions Horizon 2020 research and innovation programme under grant agreement No 665148.

* vahid.ansari@uni-paderborn.de

[1] B. Brecht, D. V. Reddy, C. Silberhorn, and M. G. Raymer, Physical Review X **5**, 041017 (2015).
[2] T. C. Ralph, I. Söllner, S. Mahmoodian, A. G. White, and P. Lodahl, Physical Review Letters **114**, 173603 (2015).
[3] J. Nunn, I. A. Walmsley, M. G. Raymer, K. Surmacz, F. C. Waldermann, Z. Wang, and D. Jaksch, Physical Review A **75**, 011401 (2007).
[4] Z. Zheng, O. Mishina, N. Treps, and C. Fabre, Physical Review A **91**, 031802 (2015).
[5] K. E. Dorfman, F. Schlawin, and S. Mukamel, The Journal of Physical Chemistry Letters **5**, 2843 (2014).
[6] B. Brecht, A. Eckstein, A. Christ, H. Suche, and C. Silberhorn, New Journal of Physics **13**, 065029 (2011).
[7] A. Eckstein, B. Brecht, and C. Silberhorn, Optics Express **19**, 13770 (2011).
[8] D. V. Reddy, M. G. Raymer, C. J. McKinstrie, L. Mejling, and K. Rottwitt, Optics Express **21**, 13840 (2013).
[9] B. Brecht, A. Eckstein, R. Ricken, V. Quiring, H. Suche, L. Sansoni, and C. Silberhorn, Physical Review A **90**, 030302 (2014).
[10] P. Manurkar, N. Jain, M. Silver, Y.-P. Huang, C. Langrock, M. M. Fejer, P. Kumar, and G. S. Kanter, (2016), 1606.07794.
[11] D. N. Fittinghoff, I. A. Walmsley, J. L. Bowie, J. N. Sweetser, R. T. Jennings, M. A. Krumbügel, K. W. DeLong, and R. Trebino, Optics Letters **21**, 884 (1996).
[12] J.-y. Zhang, A. P. Shreenath, M. Kimmel, E. Zeek, R. Trebino, and S. Link, Optics Express **11**, 601 (2003).
[13] J. Roslund, R. M. de Araújo, S. Jiang, C. Fabre, and N. Treps, Nature Photonics **8**, 109 (2014).
[14] W. P. Grice, A. B. U'Ren, and I. A. Walmsley, Physical Review A **64**, 063815 (2001).
[15] A. B. U'Ren, C. Silberhorn, K. Banaszek, I. A. Walmsley, R. K. Erdmann, W. P. Grice, and M. G. Raymer, Laser Physics **15**, 146 (2005).
[16] G. Harder, V. Ansari, B. Brecht, T. Dirmeier, C. Marquardt, and C. Silberhorn, Optics Express **21**, 13975 (2013).
[17] A. Dosseva, Ł. Cincio, and A. M. Brańczyk, Physical Review A **93**, 013801 (2016).
[18] C. K. Law, I. A. Walmsley, and J. H. Eberly, Physical Review Letters **84**, 5304 (2000).
[19] J. H. Eberly, Laser Physics **16**, 921 (2006).
[20] A. Christ, K. Laiho, A. Eckstein, K. N. Cassemiro, and C. Silberhorn, New Journal of Physics **13**, 033027 (2011).
[21] M. Avenhaus, A. Eckstein, P. J. Mosley, and C. Silberhorn, Optics Letters **34**, 2873 (2009).
[22] R. Loudon, *The Quantum Theory of Light* (OUP Oxford, 2000).
[23] W. K. Wootters and B. D. Fields, Annals of Physics **191**, 363 (1989).
[24] Bandyopadhyay, Boykin, Roychowdhury, and Vatan, Algorithmica **34**, 512 (2002).
[25] A. Monmayrant, S. Weber, and B. Chatel, Journal of Physics B: Atomic, Molecular and Optical Physics **43**, 103001 (2010).
[26] D. V. Reddy, M. G. Raymer, and C. J. McKinstrie, Optics Letters **39**, 2924 (2014).
[27] J. B. Altepeter, E. R. Jeffrey, and P. G. Kwiat, Advances in Atomic, Molecular, and Optical Physics **52**, 105 (2005).